Soft Matter

Cross-stream migration of a Brownian droplet in a polymer solution under Poiseuille flow

Journal:	*Soft Matter*
Manuscript ID	SM-ART-12-2018-002552.R1
Article Type:	Paper
Date Submitted by the Author:	15-Feb-2019
Complete List of Authors:	Howard, Michael; University of Texas at Austin, McKetta Department of Chemical Engineering Truskett, Thomas; The University of Texas at Austin, McKetta Department of Chemical Engineering Nikoubashman, Arash; Johannes Gutenberg University of Mainz, Institute of Physics

Soft Matter

ARTICLE TYPE

Cite this: DOI: 10.1039/xxxxxxxxxx

Received Date
Accepted Date

DOI: 10.1039/xxxxxxxxxx

www.rsc.org/journalname

Cross-stream migration of a Brownian droplet in a polymer solution under Poiseuille flow

Michael P. Howard[a*], Thomas M. Truskett[a], and Arash Nikoubashman[b]

The migration of a Brownian fluid droplet in a parallel-plate microchannel was investigated using dissipative particle dynamics computer simulations. In a Newtonian solvent, the droplet migrated toward the channel walls due to inertial effects at the studied flow conditions, in agreement with theoretical predictions and recent simulations. However, the droplet focused onto the channel centerline when polymer chains were added to the solvent. Focusing was typically enhanced for longer polymers and higher polymer concentrations with a nontrivial flow-rate dependence due to droplet and polymer deformability. Brownian motion caused the droplet position to fluctuate with a distribution that primarily depended on the balance between inertial lift forces pushing the droplet outward and elastic forces from the polymers driving it inward. The droplet shape was controlled by the local shear rate, and so its average shape depended on the droplet distribution.

Introduction

Particle migration in a microchannel[1,2] has important applications in separation technologies such as filtration,[3] cell sorting,[4] and fractionation.[5] It also has implications for physical processes like the margination of cells in the blood stream[6,7] and for multiphase flows in geological formations (enhanced oil recovery).[8–10] Such cross-stream migration could be desirable if a separation is needed but undesirable if a homogeneous distribution is preferred, and it is important to understand and design the conditions under which migration occurs. Multiple mechanisms exist for cross-stream migration in microchannels,[11–15] but in this article we will focus on particle migration that is passively controlled by a pressure- or gravity-driven flow,[16,17] which is attractive from an engineering perspective for its potential as a scalable, high-throughput technology.

Rigid particles in a Newtonian fluid are known to move across streamlines in parabolic (Poiseuille) flows due to lift forces at small but finite fluid inertia.[18,19] Inertial lift outward from the channel center is balanced by an inward force induced by hydrodynamic interactions with the walls, causing the particle to adopt an intermediate lateral position.[17,20,21] This effect was first observed experimentally by Segré and Silberberg,[22] who found that millimeter-sized spheres in pipe flow migrated to an annulus at roughly 60% of the pipe radius. The number and position of these "focusing" points depends on the channel geometry and flow, and has also been demonstrated for, e.g., parallel plates[23] and square ducts.[24]

Deformable droplets in a Newtonian fluid exhibit an even richer set of behaviors than their rigid counterparts.[18] Unlike rigid spheres, droplets can migrate across streamlines even in the Stokes flow (inertialess) limit due to their deformability. Chan and Leal showed that the direction of this migration depends on the viscosity ratio between the droplet and the fluid.[25] Stan et al. found that chemical and surfactant-induced Marangoni effects also influenced droplet migration.[26,27] At finite fluid inertia, Legendre and Magnaudet demonstrated that there is lift on a droplet[28] analogous to the Saffman lift on a rigid particle[29,30] but with a magnitude that depends on the viscosity ratio between the droplet and the fluid. Experiments[4,31] and simulations[32–35] have shown that droplets undergo Segré–Silberberg-type migration in Poiseuille flow, and that the preferred lateral position depends on several dimensionless parameters, including the Reynolds and capillary numbers, as recently discussed in detail by Marson et al.[35]

High-throughput applications like filtration or sorting may require focusing particles onto the channel centerline,[16,21] which is not always achieved by inertial or deformation-induced migration in simple channel geometries. Considerable efforts have been dedicated to design various microfluidic device geometries that can manipulate particles in this way,[21] but finding such geometries can be difficult and highly problem specific.[17] Fortunately, it has been shown that the addition of polymers to the Newtonian solvent provides a simple mechanism, called *viscoelastic focusing*,[36] to drive particles across streamlines toward regions of

---

[a] *McKetta Department of Chemical Engineering, University of Texas at Austin, Austin, Texas 78712, USA*

[b] *Institute of Physics, Johannes Gutenberg University Mainz, Staudingerweg 7, 55128 Mainz, Germany*

[*] *Email: mphoward@utexas.edu*

low shear.

Viscoelastic polymer solutions induce inward particle migration in Poiseuille flow due to a gradient in the first normal stress difference over the particle surface.[37] The elastic force exerted by the polymers competes directly with other forces acting on the droplet for the flow conditions, including inertial lift, deformation-induced forces, and wall forces, to set the lateral position of the particle. Such viscoelastic focusing of rigid particles has been demonstrated experimentally[10,37–42] and using computer simulations.[43–48] Interestingly, a neutral surface separating focusing points at the channel center and at the walls was discovered in simulations for certain classes of viscoelastic fluids.[43] Droplets under shear are also known to migrate in polymer solutions.[4,25,39,40]

Most prior theoretical descriptions[18,25,36,37] and simulations[43,44,48] of viscoelastic focusing have adopted a continuum-level description. Such models neglect microscopic details and fluctuations of the macromolecular components of the viscoelastic medium and the particle or droplet. However, in microfluidic and nanofluidic devices, it can be necessary to consider such motion and interactions. For example, Brownian motion leads to considerable scattering in the position of a rigid sphere around the Segré–Silberberg annulus for Poiseuille flow in a pipe.[49] Moreover, Brownian particles are often comparable in size to the macromolecular constituents of non-Newtonian fluids. At these length scales, Brownian spheres can exhibit anomolous motion in polymer solutions,[50–53] which has been attributed to coupling between the motion of the sphere and the polymers.[54,55] It is then unclear whether well-established results for viscoelastic focusing of larger particles directly transfer to smaller particles in microchannels.

We previously demonstrated the applicability of viscoelastic focusing for Brownian rigid spheres with sizes comparable to the constituent polymer chains of a viscoelastic medium.[45–47] However, we noted significant fluctuations of the particle around its focused position, in qualitative agreement with microfluidic experiments.[41] It is desirable to exploit the viscoelastic focusing mechanism to manipulate small Brownian droplets, which fluctuate in shape in addition to position, in microchannels. To our knowledge, this problem has gone relatively unexplored.

It is not obvious whether the viscoelastic focusing mechanism also applies to Brownian droplets. Unlike their rigid counterparts, small droplets deform under shear and eventually rupture at sufficiently high shear rates. The critical shear rate for this to occur depends sensitively on the droplet confinement and non-Newtonian effects in the surrounding fluid.[56–58] A droplet may breakup before sufficient elastic forces develop to focus it onto the centerline, but deformation-induced migration of the droplet,[18,25] which does not occur for rigid spheres, may actually assist the desired cross-stream migration in certain regimes. The deformability of the droplets may further lead to nontrivial coupling with comparably sized polymer chains, especially in confinement.[59] For sufficiently long polymers or high enough polymer concentrations, viscoelastic forces could induce cross-stream migration of a small Brownian droplet in a microchannel, but the distribution of the droplet position in the channel may be broad or narrow under certain flow conditions.

In this article, we test the ability of viscoelastic focusing to induce cross-stream migration of Brownian droplets using particle-based computer simulations. Although the droplet migrated outward in a Newtonian solvent (in agreement with prior simulations[35]), we found that it focused onto the channel centerline in solutions of sufficiently long polymers at modest concentrations. The flow-rate dependence of this cross-streamline migration was nontrivial due to a combination of effects from droplet deformation and the elastic force exerted by the polymers. We also varied the viscosity ratio between the droplet and the solvent, but did not observe any significant effect on the migration in the flow regime considered. The droplet shape in the parabolic flow was controlled primarily by the local shear rate (capillary number) near the droplet, and so its average shape depended sensitively on the droplet distribution in the channel.

The rest of this article is organized as follows. We first describe the simulation model, including characterization of the fluid surface tension and viscosity. We then report our results, first analyzing the simulated flow fields and then systematically demonstrating the effects of polymer concentration, polymer chain length, and flow rate on the distribution of the droplet in the channel and its shape. We finally present our conclusions, suggesting avenues for future inquiry.

Simulation model

A single fluid droplet was simulated in a Newtonian solvent and in a polymer solution using dissipative particle dynamics (DPD) simulations[60–62] DPD is a particle-based mesoscale simulation method that faithfully resolves hydrodynamic interactions, incorporates thermal fluctuations, and is well-suited for modeling multiphase fluids. In DPD, particles interact with each other through three pairwise forces: a conservative force $\mathbf{F}_\mathrm{C}$, a dissipative force $\mathbf{F}_\mathrm{D}$, and a random force $\mathbf{F}_\mathrm{R}$. As is typical, we modeled the conservative force acting on particle i due to particle j by a soft repulsion,[62]

$$\mathbf{F}_\mathrm{C} = \begin{cases} a_{ij}\,(1 - r/r_\mathrm{c})\,\hat{\mathbf{r}} & r \le r_\mathrm{c} \\ 0 & r > r_\mathrm{c} \end{cases}, \tag{1}$$

where a_{ij} sets the strength of the repulsion between particles i and j, r is the distance between the particle centers, $\hat{\mathbf{r}}$ is the unit vector to the center of particle i from the center of particle j, and r_c is the cutoff radius for the interaction that sets the effective size of the particles.

The random and dissipative forces impart thermal fluctuations and drag while also acting as a thermostat on the DPD particles. These forces are applied in a pairwise manner that conserves momentum, with the forces on particle i from particle j given by

$$\mathbf{F}_\mathrm{D} = -\gamma_{ij} w(r)(\hat{\mathbf{r}} \cdot \Delta\mathbf{v})\hat{\mathbf{r}} \tag{2}$$

$$\mathbf{F}_\mathrm{R} = \sqrt{\gamma_{ij} w(r)}\,\xi\,\hat{\mathbf{r}}, \tag{3}$$

where γ_{ij} is the drag coefficient between particles i and j, w is a weight function, and $\Delta\mathbf{v} = \mathbf{v}_i - \mathbf{v}_j$ is the difference in the velocities of particles i and j. To satisfy the fluctuation–dissipation theorem,[61] ξ is an independent random variable for each pair of particles that has zero mean, $\langle \xi(t) \rangle = 0$, and a variance $\langle \xi(t)\xi(t') \rangle = 2k_{\mathrm{B}}T\delta(t-t')$ with k_{B} being Boltzmann's constant and T being the temperature. In this work, the drag coefficients were assigned per particle, γ_i, and the effective drag coefficient for a pair was determined by the mixing rule $\gamma_{ij} = 2/(1/\gamma_i + 1/\gamma_j)$.[63]

The weight function w modulates the dynamic properties, i.e., diffusivity and viscosity, of the fluid. We used the generalized weight function proposed by Fan et al.,[64]

$$w(r) = \begin{cases} (1-r/r_{\mathrm{c}})^s & r \le r_{\mathrm{c}} \\ 0 & r > r_{\mathrm{c}} \end{cases}, \tag{4}$$

with $s = 1/2$. This choice of s increases the Schmidt number of the fluid compared to the standard DPD weight function[62] ($s = 2$) to give a value closer to that of a real liquid. We also found that using $s = 1/2$ gave better agreement with the no-slip boundary conditions at the microchannel walls than using $s = 2$ (see below).

Fluid model

The polymer solution and droplet were modeled using three types of DPD particles: solvent (s) particles, polymer segment (p) particles, and droplet (d) particles. The model and results in this article will be reported in a fundamental system of units using d as the unit of length, m as the unit of mass, and ε as the unit of energy, which gives $\tau = \sqrt{md^2/\varepsilon}$ as the unit of time. Throughout, the total density of DPD particles was $\rho = 3.0/d^3$, all DPD particles had equal mass $1.0m$, the temperature was $T = 1.0\,\varepsilon/k_{\mathrm{B}}$, and the cutoff radius was $r_{\mathrm{c}} = 1.0\,d$. All simulations were performed using HOOMD-blue[65–67] (version 2.2.5) on multiple graphics processing units with a simulation time step of $0.01\,\tau$.

In order to choose the DPD repulsive parameters, we first computed the surface tension σ between coexisting slabs of solvent and droplet particles. We fixed the repulsive parameter for particles of the same type to standard DPD values,[62] $a_{\mathrm{ss}} = a_{\mathrm{dd}} = 25\,\varepsilon/d$, but varied the cross-interaction strength, a_{sd}. The drag coefficient should not affect the measured surface tension, which is a static property, and so was fixed to $\gamma_{\mathrm{s}} = \gamma_{\mathrm{d}} = 1.0\,m/\tau$ to promote fast diffusion. The coexisting slabs were equilibrated by joining two cubic regions of edge length $30\,d$ to give an orthorhombic box centered around the origin with edge lengths $L_x = 30\,d$, $L_y = 30\,d$, and $L_z = 60\,d$, where x, y, and z denote the Cartesian coordinate axes. Particles were allowed to interdiffuse for $5 \times 10^4\,\tau$ to equilibrate the joined slabs.

In this geometry, σ can be computed from the pressure anisotropy,[68,69]

$$\sigma = \frac{L_z}{2}\left\langle p_{zz} - \frac{p_{xx}+p_{yy}}{2} \right\rangle, \tag{5}$$

where $p_{\alpha\alpha}$ denotes the diagonal component of the stress tensor for index α, and the prefactor of 1/2 accounts for the presence of two interfaces due to the periodic boundary conditions. The cross-interaction strength was varied from $a_{\mathrm{sd}} = 40\,\varepsilon/d$ to $100\,\varepsilon/d$, and the surface tension was measured using eq. (5) by sampling $p_{\alpha\alpha}$ every $0.05\,\tau$ during a $10^5\,\tau$ simulation. The measured surface tension (Fig. 1) is in good agreement with Groot and Warren's empirical equation,[62]

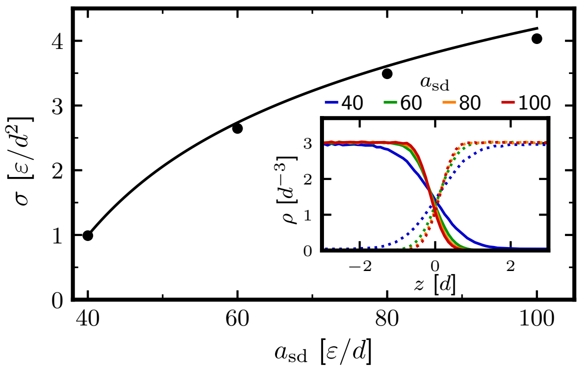

Fig. 1 Surface tension σ between slabs of solvent and droplet particles for varied strengths of the repulsive cross-interaction a_{sd}. The solid line gives the value predicted by eq. (6). Inset: Density ρ of solvent (solid lines) and droplet (dashed lines) particles near the fluid interface at $z = 0\,d$.

$$\sigma = 0.75\rho k_{\mathrm{B}}Tr_{\mathrm{c}}\chi^{0.26}(1-2.36/\chi)^{3/2}, \tag{6}$$

with $\chi = 0.286(a_{\mathrm{sd}} - a_{\mathrm{ss}})$ being their fit to the Flory–Huggins parameter for the binary DPD fluid when $\rho = 3.0/d^3$.

As expected, the surface tension increased with increasing a_{sd} because the solvent and droplet particles became less miscible. The solvent and droplet particle density profiles near the interface (inset of Fig. 1) converged to similar values with increasing a_{sd}, developing a sharper interface as σ increased. We desired a droplet fluid that was barely soluble in the solvent but that formed a droplet that could still deform under the flow rates accessible in the simulations. At $a_{\mathrm{sd}} = 60\,\varepsilon/d$, the density of solvent particles dissolved in the droplet phase was already small ($4.66 \times 10^{-4}/d^3$), the interfacial width was comparable to the DPD particle diameter, and the surface tension $\sigma = 2.65\,\varepsilon/d^2$ permitted modest deformation under viable flow rates. We accordingly selected $a_{\mathrm{sd}} = 60\,\varepsilon/d$ for the cross-interaction strength.

We subsequently measured the shear viscosity of the solvent using reverse nonequilibrium simulations (RNES).[70] Details of this method are well-described elsewhere.[70,71] We simulated a cubic box of edge length $20d$ containing only solvent particles with drag coefficients that varied from $\gamma_{\mathrm{s}} = 1.0\,m/\tau$ to $50.0\,m/\tau$. Using RNES, we imposed a shear stress τ_{zx} on the solvent by periodically exchanging the x-momenta of one pair of particles from slabs of width $1.0\,d$ centered at $z = \pm 5\,d$. The swapped particles were the ones that most opposed the desired direction of flow (x) in each slab. We measured the velocity profile $u_x(z)$ between the exchange slabs ($|z| < 3.5\,d$) every $10\,\tau$ over a $5 \times 10^5\,\tau$ simulation, obtaining a Couette flow profile with a shear rate $\dot{\gamma} = \partial u_x/\partial z$ that decreased as the time between exchanges was increased from $0.05\,\tau$ to $0.5\,\tau$. The imposed shear stress was proportional to the measured shear rate, $\tau_{zx} = \mu_{\mathrm{s}}\dot{\gamma}$, as expected for a Newtonian fluid. The shear viscosity, μ_{s}, was then determined by a linear fit of τ_{zx} versus $\dot{\gamma}$.

As expected, the viscosity increased with increasing γ_{s} (Fig. 2).

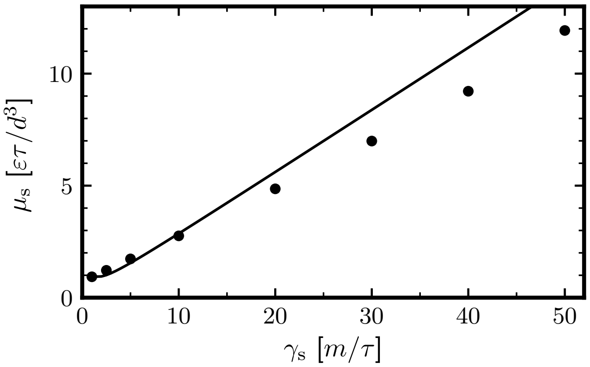

Fig. 2 Solvent viscosity μ_s for varied drag coefficient γ_s. The solid line gives the value predicted by eq. (7).

The simulated viscosity was generally lower than theoretically estimated,[64]

$$\mu_s = \frac{315 k_B T}{128\pi\gamma_s r_c^3} + \frac{512\pi\gamma_s \rho^2 r_c^5}{51975}, \tag{7}$$

particularly at high values of γ_s. We selected $\gamma_s = 4.5\,m/\tau$ for the solvent particles, which gives a measured shear viscosity of $\mu_s = 1.73\varepsilon\tau/d^3$. In most cases, we used $\gamma_d = \gamma_s$, giving a droplet viscosity $\mu_d = \mu_s$, but we also varied γ_d to determine the effects of the viscosity ratio in select cases.

To model linear polymer chains of length M that were fully soluble in the solvent but insoluble in the droplet, the polymer segment (p) particles were treated as if they were solvent (s) particles in the DPD interactions, i.e., $a_{pp} = a_{ps} = 25\,\varepsilon/d$, $a_{pd} = 60\,\varepsilon/d$, and $\gamma_p = 4.5\,m/\tau$. Bonds within a chain were modeled by adding a harmonic spring force $\mathbf{F}_B$ to $\mathbf{F}_C$ for connected pairs of particles. The force on particle i bonded to particle j was

$$\mathbf{F}_B = -\kappa(r-b)\,\hat{\mathbf{r}}, \tag{8}$$

with spring constant $\kappa = 100\,\varepsilon/d^2$ and $b = 0.7\,d$.[72]

Flow in microchannel

We simulated pressure-driven flow of the droplet and polymer solution in a parallel plate microchannel. The full system was initialized as follows. We first dispersed solvent particles with a total density of $\rho = 3.0/d^3$ into a three-dimensional, periodic simulation box of dimensions $L_x = 80\,d$, $L_y = 40\,d$, and $L_z = 42\,d$ and equilibrated the solvent for $1000\,\tau$. We chose x as the direction of flow in the microchannel, and the parallel plates had normals along z. We constructed the microchannel walls by freezing solvent particles having $|z| \ge H = 20d$, zeroing their velocities, and switching their types to be wall (w) particles.[73,74] (The total channel width was $2H$.) The wall particles interacted with the fluid as if they were solvent particles, i.e., $a_{sw} = a_{pw} = 25\,\varepsilon/d$, $a_{dw} = 60\,\varepsilon/d$, and $\gamma_w = 4.5\,m/\tau$. Mutual DPD interactions between wall particles were excluded. To help enforce no-slip and no-penetration boundary conditions at the walls, solvent, polymer, and droplet particles were additionally reflected from the planes at $z = \pm H$ using bounce-back rules.[74,75] These boundary conditions on the individual polymer beads ensure that the polymer chains do not cross through the walls.

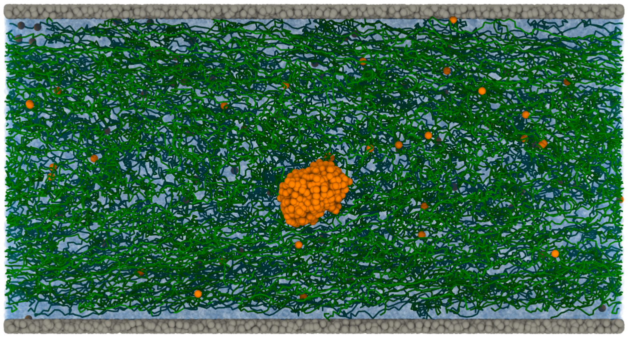

Fig. 3 Fluid droplet (orange) in a parallel plate microchannel (gray) with $f_x = 0.005\,\varepsilon/d$. Polymers of length $M = 80$ at polymer weight fraction $\phi_p = 10\%$ are depicted in green. The solvent particles (blue) have been removed from the front of the image for visual clarity. A small number of droplet particles are dissolved in the polymer solution due to their finite solubility. This snapshot was rendered using OVITO 2.9.0.[76]

We selected particles near the origin of the channel to form a droplet of radius $R = 4.0d$, giving a droplet blockage ratio of $R/H \approx 0.2$. Due to the small but finite solubility of the droplet particles in the solvent, we first estimated the number of particles required to form such a droplet volume using the lever rule with the coexistence densities shown in Fig. 1. This procedure gave a droplet with a radius initially larger than R, but some particles later dissolved into the solvent so that the droplet reached its target radius. We then randomly created linear polymers of length M from the remaining solvent particles. To build each chain, we first randomly removed M solvent particles. They were reinserted as polymer segment (p) particles between the channel walls in a randomly generated chain conformation having a bond length of $0.7\,d$ between connected particles. The number of polymer chains N_p was chosen to give the desired polymer weight fraction, $\phi_p = N_p M/\rho V$, where $V = 2L_x L_y H$ is the volume of the microchannel. In most simulations, we used $\phi_p = 5.0\%$ or 10.0%, but also tested $\phi_p = 0.0\%$ (no polymer), 2.5% and 7.5% for selected conditions. The complete configuration, including the solvent, droplet, and polymers, was equilibrated for $5000\,\tau$.

Flow was generated by applying a constant body force, f_x, in the x-direction for all solvent, polymer, and droplet particles. For the pure solvent, applying such a force in conjunction with no-slip boundary conditions at the channel walls gives the standard parabolic (Poiseuille) velocity field,

$$u_x(z) = U\left[1 - \left(\frac{z}{H}\right)^2\right], \tag{9}$$

where $U = \rho f_x H^2/2\mu_s$ is the maximum velocity at the channel centerline for this flow field. To help enforce the wall boundary conditions in the simulations, the frozen wall particles were assigned velocities $v_x(z) = -u_x(2H - |z|)$ based on their positions in the wall.[74] Additionally, $u_x(z)$ was initially superimposed onto the polymer solution and droplet to accelerate the approach to a steady flow profile during a $5000\,\tau$ simulation. Fig. 3 shows an example configuration for the polymer solution under flow at steady state.

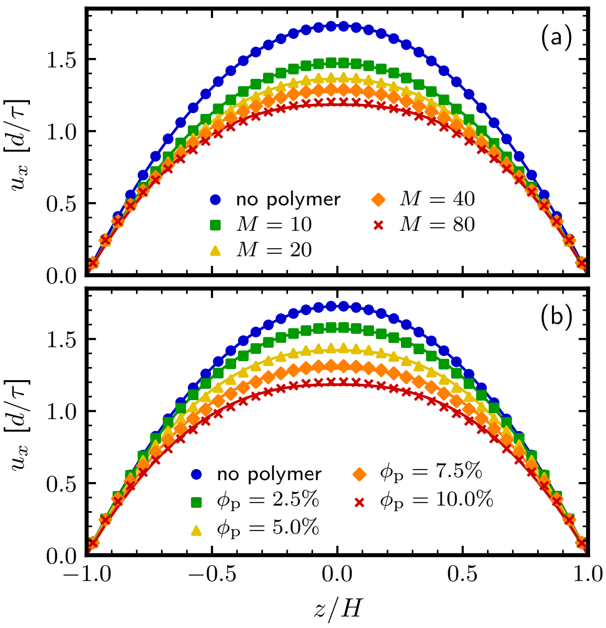

Fig. 4 Average flow profile in the microchannel, u_x, at $f_x = 0.005\,\varepsilon/d$ for (a) various polymer chain lengths at $\phi_p = 10.0\%$ and (b) various concentrations of $M = 80$ polymers. The solid lines give the expected profile according to eq. (9) without any fitting parameters for the no-polymer case and the fitted profiles from eq. (11) for the polymer solutions. Note that the circles and crosses display the same data in both panels.

We repeated this procedure 5 times for each combination of chain length M, polymer concentration ϕ_p, body force f_x, and droplet viscosity μ_d studied to generate independent starting configurations. Production simulations of $10^5\,\tau$ were performed for each configuration. The droplet properties were sampled every $50\,\tau$, while the properties of the entire solution were recorded every $2500\,\tau$. The computational workflow and data were managed using the signac framework.[77]

Results and discussion

Flow field

We first measured the average velocity profile in the microchannel, including the solvent, polymers, and droplet, to characterize the flow field and check for the anticipated non-Newtonian effects in the polymer solutions. The flow was unidirectional, $u_x(z)$, and is shown for various polymer chain lengths at the largest polymer concentration simulated ($\phi_p = 10.0\%$) in Fig. 4a and for various concentrations of the longest polymers simulated ($M = 80$) in Fig. 4b. The body force in Fig. 4 was $f_x = 0.005\,\varepsilon/d$, which was the largest value we simulated and where any wall slip or non-Newtonian flow effects should be most pronounced. This upper bound for f_x in our simulations was determined by trial and error so that no droplet breakup occurred.

The velocity profile in the absence of polymer was parabolic, as expected, and was also in quantitative agreement with eq. (9) using the measured μ_s (Fig. 2). This indicates that the no-slip boundary conditions are well-enforced and also validates the RNES measurement of μ_s. The presence of the droplet made no measurable contribution to the expected neat solvent flow field; however, the addition of polymers with $M = 10$ resulted in a lower maximum velocity U at the centerline, consistent with the expected higher viscosity of a polymer solution (Fig. 4a).[78] Increasing the length of the polymers from $M = 10$ to $M = 80$ further lowered U. Similar trends were observed when varying the concentration of the $M = 80$ polymers from $\phi_p = 0.0\%$ to 10.0% (Fig. 4b), with higher polymer concentrations giving lower U.

For dilute polymer solutions, the zero-shear viscosity μ_0 can be estimated using Einstein's equation for the viscosity of a suspension,[79,80]

$$\mu_0 = \mu_s(1 + 2.5\Phi), \tag{10}$$

where $\Phi = 4\pi R_h^3 N_p/3V$ is the polymer pervaded-volume fraction defined using the hydrodynamic radius R_h of the polymers. For simplicity, we approximate the polymers as Gaussian chains, for which $R_h \approx 0.271 b M^{1/2}$.[81] This yields an estimated viscosity increase of roughly 5% for the $M = 80$ polymers at $\phi_p = 2.5\%$ and of nearly 20% for the same polymers at $\phi_p = 10.0\%$. Using this estimate as an effective viscosity in eq. (9) gives a maximum velocity that almost quantitatively matches the measured value in Fig. 4b at $\phi_p = 2.5\%$, but overpredicts the maximum velocity at $\phi_p = 10.0\%$.

The discrepancy at the higher concentration was partially caused by the increasingly non-Newtonian character of the polymer solutions. As the polymer length or concentration increased, the velocity profiles became less parabolic and developed a flattened region near $z/H = 0$. Unlike the neat solvent, the velocity profiles for the polymer solutions were not well-described using eq. (9), which was derived for a Newtonian fluid, because of this difference in shape. To obtain a better fit to the velocity profiles and quantify this non-Newtonian behavior, we assumed that the shear stress in the polymer solutions followed a power-law model, $\tau_{zx} = K\dot{\gamma}^n$, where n is the flow behavior index and K is a prefactor that also gives correct dimensions to τ_{zx}. In a parallel plate channel, the flow field for a power-law fluid is

$$u_x(z) = \frac{n}{n+1}\left(\frac{\rho f_x H^{n+1}}{K}\right)^{1/n}\left[1 - \left(\frac{|z|}{H}\right)^{1+1/n}\right]. \tag{11}$$

A Newtonian solvent has $n = 1$ and $K = \mu_s$, and eq. (11) reduces to eq. (9), whereas shear-thinning fluids have $n < 1$, resulting in a non-parabolic flow profile.

We determined K and n by fitting the flow fields in Fig. 4 through eq. (11), recovering exponents ranging from $n = 0.92$ for $M = 10$ (nearly Newtonian) to $n = 0.66$ for $M = 80$ (shear thinning) when $\phi_p = 10.0\%$ (Fig. 4a). Likewise, n decreased from 0.81 at $\phi_p = 2.5\%$ to 0.69 at $\phi_p = 7.5\%$ for the $M = 80$ polymers (Fig. 4b). Hence, the polymer solutions became increasingly shear-thinning for longer polymers or higher polymer concentrations, as expected. There is a small but noticeable deviation of the measured velocity from the fit using eq. (11) for $M = 80$ at $\phi_p = 10.0\%$, suggesting that the shear stress may have a more sophisticated functional form than the simplistic power-law model. Nonetheless, the fitted exponents give us a useful qualitative characterization of the polymer solutions.

Solutions of longer polymer chains shear thin more readily under flow than solutions with shorter chains because longer chains have longer relaxation times, τ_p, that cause them to deform and align with the flow at smaller $\dot{\gamma}$.[82] The dimensionless Weissenberg number, $\mathrm{Wi} = \dot{\gamma}\tau_p$, characterizes this relationship. When $\mathrm{Wi} \ll 1$, the rate of deformation is slow compared to the polymer relaxation and primarily coil conformations are expected, whereas for $\mathrm{Wi} \gg 1$, the polymers are expected to be highly deformed. We approximate the shear rate by $\dot{\gamma} \approx U/H$, and estimate the polymer relaxation time from the Zimm model for a Gaussian chain,[81,82] $\tau_p \approx 0.326\mu_s b^3 M^{3/2}/k_B T$. We find that $\mathrm{Wi} \approx 0.4$ for the $M = 10$ polymers and $\mathrm{Wi} \approx 8$ for the $M = 80$ polymers for the conditions in Fig. 4a ($f_x = 0.005\,\varepsilon/d$). Hence, more significant chain stretching and shear-alignment is expected for the longer chains, which should result in more shear thinning (smaller values of n). This expectation is consistent with the shape of the flow fields in Fig. 4 and the fitted values for n. The enhanced shear thinning corresponds to more significant chain stretching, which should lead to stronger elastic forces on the droplet for cross-stream migration.

Droplet distribution

Having characterized the flow in the microchannel, we measured the center-of-mass position of the droplet between the channel walls, z_c. The droplet was identified for each configuration using a clustering procedure[83,84] in order to exclude droplet particles dissolved in the solvent from subsequent analysis. We analyzed the absolute value $|z_c|$ based on the symmetry of the microchannel and to improve sampling. Previous studies[34,35] have reported the average center-of-mass position, $\langle |z_c| \rangle$, which is the first moment of the distribution of $|z_c|$. However, a Brownian droplet can adopt a variety of distributions in the channel depending on the conditions, and we found that $\langle |z_c| \rangle$ was not sufficiently discriminating between these. For example, a uniformly distributed droplet has $\langle |z_c| \rangle \approx (H-R)/2$, which is indistinguishable from a droplet which is strongly focused at this position throughout the entire simulation. We accordingly computed the distribution of $|z_c|$ using a bin size of $1.0d$, and will focus most of our discussion around such distributions.

We first considered the distribution of the droplet in solutions of $M = 80$ polymer chains of increasing concentration ϕ_p (Fig. 5) for the flow conditions shown in Fig. 4b. In the neat solvent, the droplet migrated outward from the channel centerline, showing a strongly preferred position of $|z_c|/H \approx 0.375$. Such outward migration is consistent with prior theoretical and simulation work for droplets.[33–35] The droplet can migrate by two mechanisms: (1) deformation due to the flow, even in the creeping flow limit, and (2) lift forces at finite inertia. We define a channel Reynolds number, $\mathrm{Re} = 2\rho U H/\mu_s$, and a droplet Reynolds number $\mathrm{Re_d} = \mathrm{Re}(R/H)^2$.[21,35] When the channel Reynolds number is sufficiently small, the flow is expected to be laminar. When $\mathrm{Re_d}$ is small, inertial forces on the droplet are not significant and results from the Stokes flow limit are expected to apply. As an upper bound, we find $\mathrm{Re} \lesssim 100$ and $\mathrm{Re_d} \lesssim 4$ for the investigated flow rates, consistent with the laminar flow of Fig. 4 but suggesting that inertial lift on the droplet may be significant, as in the Segré–Silberberg effect for rigid particles.[22,47,49] This estimate is in accord with the observed migration of the droplet away from the centerline.

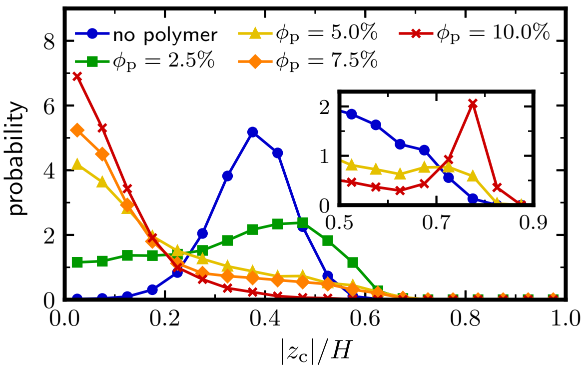

Fig. 5 Distribution of droplet center-of-mass, $|z_c|$, in a solution of $M = 80$ polymers at increasing polymer concentrations ϕ_p for $f_x = 0.005\,\varepsilon/d$. The inset shows the same distribution near the channel wall at the lowest flow rate simulated ($f_x = 0.001\,\varepsilon/d$), where a pronounced peak develops at larger ϕ_p due to depletion interactions. Note that the axis markings for $|z_c|/H$ have been chosen so that they can be readily reinterpreted in units of the droplet blockage ratio, $R/H = 0.2$.

The addition of polymers to the channel at increasing polymer concentration ϕ_p dramatically altered the preferred position of the droplet. The droplet distribution significantly broadened at the lowest concentration ($\phi_p = 2.5\%$). Interestingly, this included an increased probability of finding the droplet near the wall, beyond the preferred peak in the neat solvent, which we speculate may be partially due to polymer-mediated depletion interactions.[85] Depletion, often discussed in the context of rigid spherical colloids in solution with smaller polymer chains, induces an effective attraction between otherwise hard particles (the colloids) due to volume exclusion of a secondary species (the polymers).[86] In this case, the effective attraction is between the droplet and the wall because the polymers are insoluble in the droplet and cannot penetrate the channel boundaries.

Continuing to add polymer increasingly focused the droplet onto the channel centerline with a narrowing distribution of $|z_c|$. The increased polymer concentration had competing effects on the droplet migration. On the one hand, the depletion force scales with ϕ_p,[85] which increases the outward force on the droplet near the wall. On the other hand, the increased ϕ_p lowered the maximum velocity in the channel, decreasing the outward inertial lift on the droplet.[21] Concurrently, the increased polymer concentration also increased the inward elastic force on the droplet.[47] The net result of these interactions when $f_x = 0.005\,\varepsilon/d$ was an increased inward force for larger ϕ_p, which improves the droplet focusing onto the centerline, consistent with our previous work on viscoelastic focusing of rigid particle.[45–47] However, the depletion attraction should also be present for systems at lower flow rates or at rest, where it may have a much larger magnitude relative to the elastic force. Indeed, a pronounced peak near the wall was also obtained at $\phi_p = 10.0\%$ as a result of depletion forces for simulations at $f_x = 0.001\,\varepsilon/d$, the lowest flow rate studied here (inset of Fig. 5).

We next considered the impact of chain length M on droplet migration at two polymer concentrations, $\phi_p = 5.0\%$ and $\phi_p = 10.0\%$.

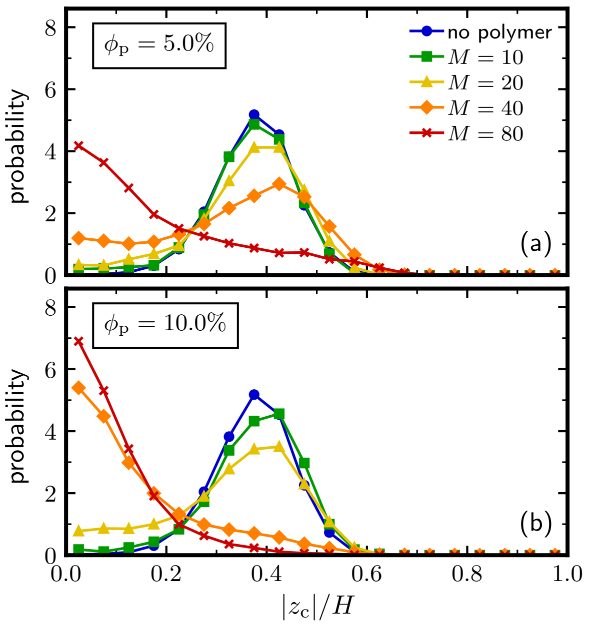

Fig. 6 Distribution of droplet center-of-mass, $|z_c|$, in a solution of polymers of length M at (a) $\phi_p = 5.0\%$ and (b) $\phi_p = 10.0\%$ for $f_x = 0.005\,\varepsilon/d$.

Longer chains are expected to have better droplet focusing onto the centerline for three reasons: (1) the elastic force should scale with M,[47] (2) longer chains deform at lower shear rates and so can exert more elastic force for a given $\dot{\gamma}$, and (3) the maximum velocity was found to be lower for longer chains, reducing the outward inertial lift. The measured distributions of $|z_c|$ (Fig. 6) are clearly consistent with this hypothesis. The addition of polymers with $M = 10$ did not have a significant impact on the droplet distribution compared to the neat solvent. This may not be surprising given that $\mathrm{Wi} = 0.4$ for the $M = 10$ polymers, and the solution is nearly Newtonian. However, adding polymers of increasing length improved the focusing onto the centerline in a monotonic fashion for a given concentration. These longer polymers have a larger Wi for a given $\dot{\gamma}$, and so stretch more and impart a larger elastic force onto the droplets.

We note, however, that there are additional concentration effects that influenced when polymers of a given size became effective focusers. This is most apparent for the $M = 40$ chains. At $\phi_p = 5.0\%$, the droplet had a broad distribution of $|z_c|$ and a most probable position of $|z_c|/H \approx 0.425$. However, at $\phi_p = 10.0\%$, the droplet was strongly focused onto the centerline. We speculate that this difference in behavior is due to an increase in elastic force with concentration, which was sufficient to overcome the inertial lift at $\phi_p = 10.0\%$ but too weak at $\phi_p = 5.0\%$.

To understand this flow rate and concentration dependence in more detail, we computed the droplet distribution for the $M = 40$ chains at varying f_x for $\phi_p = 5.0\%$ and 10.0%, which we compare to the distributions without any polymer (Fig. 7). Without polymer, the droplet initially migrated outward as f_x increased, but the peak of this distribution moved inward with additional increases in f_x (Fig. 7a), consistent with the simulations of Marson et al.[35] The initial outward migration is analogous to the Segré–Silberberg effect for rigid colloids;[47,49] however, the inward trend of the preferred position with increasing f_x is stronger for the droplet due to it deformability.[35]

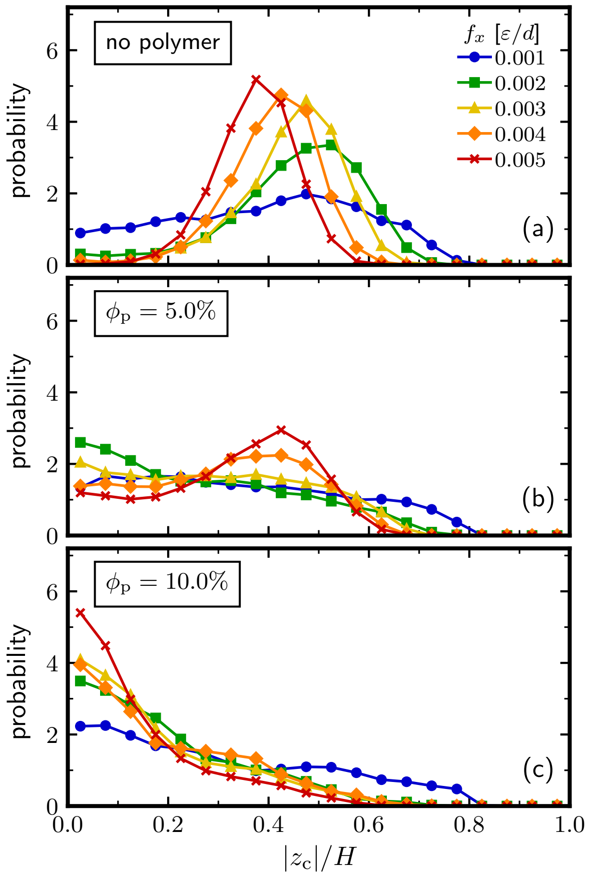

Fig. 7 Distribution of droplet center-of-mass, $|z_c|$, in a solution of $M = 40$ polymers at (a) $\phi_p = 5.0\%$ and (b) $\phi_p = 10.0\%$ for $f_x = 0.005\,\varepsilon/d$.

At $\phi_p = 5.0\%$ (Fig. 7b), there was an initial trend to migrate inward when $f_x \lesssim 0.003\,\varepsilon/d$. However, at larger f_x, the droplet began to move outward, suggesting that inertial lift dominated over the available elastic force. In contrast, the droplet distribution sharpened around the channel centerline at $\phi_p = 10.0\%$ for all f_x considered here (Fig. 7c). It is possible that there is a sufficiently large f_x that could exceed the inward elastic force at this concentration. However, the droplet may breakup under shear before such a force can be applied. This contrasts with the case of the rigid colloid, which does not have this restriction on the flow rate.

We finally tested the sensitivity of viscoelastic focusing to the viscosity ratio between the droplet and the solvent. In the Stokes flow limit, Chan and Leal showed that inward or outward droplet migration can be obtained in a Newtonian solvent based on this ratio.[25] However, recent simulations by Marson et al. suggest that such differences may not be as significant in the inertial regime.[35] Our primary interest is in how the droplet migration may change in a non-Newtonian polymer solution. We varied the droplet viscosity ratio with the solvent, μ_d/μ_s, from 0.54 ($\gamma_d = 1.0\,m/\tau$) to 5.3 ($\gamma_d = 40.0\,m/\tau$) for the $M = 80$ polymer solutions at $\phi_p = 10.0\%$, which focused the droplet when $\mu_d/\mu_s = 1.0$.

Since the effective viscosity of the polymer solution μ_0 is higher than that of the pure solvent, $\mu_\mathrm{d}/\mu_\mathrm{s}$ should be considered an upper bound on the viscosity ratio between the droplet and the polymer solution.

We found no significant differences between the droplet distributions under these conditions, and so we omit the data here for brevity. This result may not be unexpected given the qualitative picture of the viscoelastic focusing mechanism. The polymers are insoluble in the droplet, and so they primarily influence the fluid around it. (The flow inside the droplet is affected by μ_d, but such effects may be secondary.) Given that the viscosity ratio did not significantly alter the droplet distribution in the inertial regime of the pure solvent for Marson et al.,[35] it is then not surprising that the viscosity ratio also does not significantly change the droplet distribution in the polymer solution. Indeed, letting $\mu_\mathrm{d}/\mu_\mathrm{s} \to \infty$ should recover the rigid particle limit of viscoelastic focusing to which we have already drawn comparison. However, we do anticipate that the viscosity ratio may still influence the droplet distribution more significantly in other flow regimes (e.g., Stokes flow limit) that were not accessible to us in our simulations. In these cases, the migration forces controlled by the viscosity ratio, with inward or outward direction,[25] would either work cooperatively or antagonistically with the elastic force of a sufficiently deformed polymer.

Droplet shape

We have concentrated our discussion thus far on how polymers influence the droplet distribution in the microchannel, but have not yet considered how the polymers influence the droplet shape and orientation in the flow. To characterize the droplet shape, we first computed its gyration tensor $\mathbf{G}$,

$$G_{\alpha\beta} = \frac{1}{N_\mathrm{d}} \sum_{i=1}^{N_\mathrm{d}} \Delta r_{i,\alpha} \Delta r_{i,\beta}, \tag{12}$$

where $\Delta\mathbf{r}_i$ is the vector from the droplet center of mass to particle i, α and β are indices in the usual tensor notation, and N_d is the number of particles in the droplet. We then computed the eigenvalues λ_α^2 of $\mathbf{G}$, whose corresponding eigenvectors give the principal moments of the droplet, and sorted them in descending order, $\lambda_1^2 \ge \lambda_2^2 \ge \lambda_3^2$. We determined the Taylor deformation parameter,[87,88] a dimensionless measure of the asphericity of the droplet, as

$$D \approx \frac{\lambda_1 - (\lambda_2 + \lambda_3)/2}{\lambda_1 + (\lambda_2 + \lambda_3)/2}. \tag{13}$$

For a sphere, $\mathbf{G}$ is diagonal ($\lambda_1 = \lambda_2 = \lambda_3$) and $D = 0$, while a prolate spheroid has $\lambda_1 > \lambda_2 = \lambda_3$ and $D \to 1$ when the aspect ratio between the major and minor axes of the spheroid increases. Hence, larger values of D correspond to droplets that have more significant deformation. We additionally determined the inclination angle of the droplet relative to the flow direction, θ, using $\mathbf{G}$:[89]

$$\tan(2\theta) = \frac{2G_{xz}}{G_{xx} - G_{zz}}. \tag{14}$$

$\theta \approx 0^\circ$ for a sphere (no preferred orientation) or for an object completely aligned with the flow, but $\theta \neq 0^\circ$ for particles that align with a relative tilt.

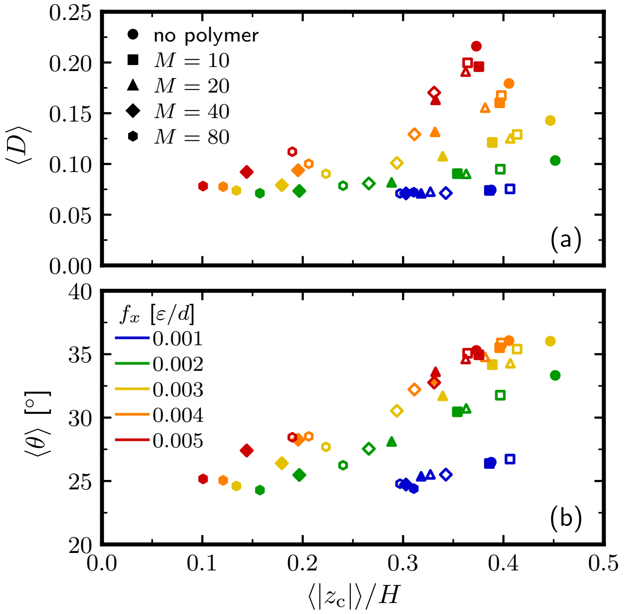

Fig. 8 Average droplet (a) Taylor deformation parameter $\langle D \rangle$ and (b) inclination angle $\langle \theta \rangle$ versus average center-of-mass position $\langle |z_\mathrm{c}| \rangle$ for varied polymer chain lengths M at $\phi_\mathrm{p} = 5.0\%$ (open symbols) and 10.0% (filled symbols). Each color indicates a different applied force f_x.

It is well-established that D increases with $\dot\gamma$ for a droplet in an unbounded shear flow.[87,88,90] In the limit of small deformations, Taylor predicted that[87,88]

$$D = \frac{19\lambda + 16}{16\lambda + 16}\mathrm{Ca}, \tag{15}$$

where $\mathrm{Ca} = \dot\gamma R \mu_0/\sigma$ is the capillary number and $\lambda = \mu_\mathrm{d}/\mu_0$ is the viscosity ratio. Roscoe[91] and Chaffey and Brenner[92] later showed that in this regime, the droplet inclination angle θ to $O(D)$ is, in radians,

$$\theta = \frac{\pi}{4} - \frac{D}{5}(2\lambda + 3). \tag{16}$$

For small deformations, $\theta \approx 45^\circ$, as argued by Taylor,[87,88] but θ decreases as the droplet deforms and aligns more with the flow for larger Ca. In Poiseuille flows, the shear rate $\dot\gamma$ (and so also the local capillary number) varies across the channel, and accordingly, the droplet may experience a different deformation and orientation based on its lateral position. There may additionally be confinement and non-Newtonian effects on the droplet deformation and orientation.[56–59,93,94]

Fig. 8a shows the average deformation $\langle D \rangle$ versus the average center-of-mass position of the droplet $\langle |z_\mathrm{c}| \rangle$, clearly indicating that the droplet is (on average) more deformed when it is (on average) farther from the centerline, where the shear rate is higher. The droplet is additionally (on average) more inclined relative to the flow when it is more deformed (Fig. 8b). This increasing average inclination is somewhat surprising, as prior studies on the deformation of droplets in simple shear flow showed that droplets are more aligned with the flow under higher shear rates,[93,94] in qualitative agreement with the predictions of eq. (16).

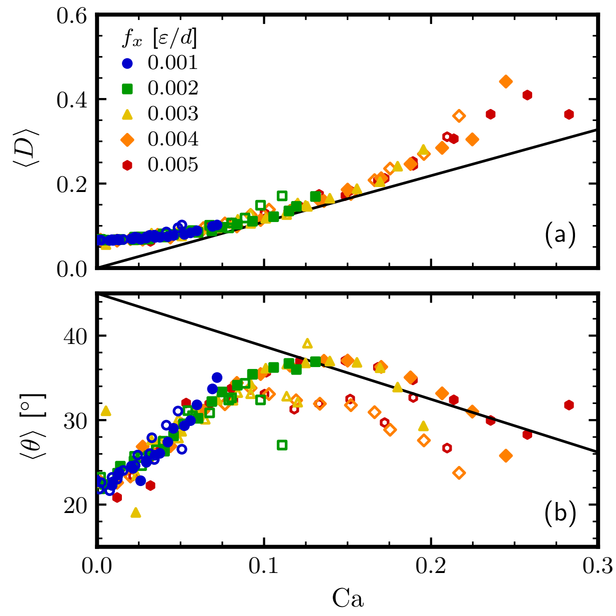

Fig. 9 Average droplet (a) Taylor deformation parameter $\langle D \rangle$ and (b) inclination angle $\langle \theta \rangle$ versus local capillary number Ca at the droplet center-of-mass for the neat solvent (closed symbols) and $M = 80$ polymers with $\phi_\mathrm{p} = 10.0\%$ (open symbols). The solid line in (a) indicates Taylor's prediction[87,88] for D with $\lambda = 1$ (eq. (15)), while the line in (b) is the small-deformation prediction[91,92] for θ with $\lambda = 1$ (eq. (16)).

It is tempting to find a parameter to collapse the data in Fig. 8 onto a single curve, e.g., through the capillary number.[35,90,95] Unfortunately, such an analysis is again considerably complicated using only average quantities because of the droplet distribution. Indeed, the average properties computed in Fig. 8 and in prior studies[35] are intimately connected to the droplet distribution, which sets the preferred droplet location and as a consequence, the shear rates it experiences. This interplay between the droplet distribution and its shape may be the reason for the increase in $\langle \theta \rangle$ with increasing $\langle |z_\mathrm{c}| \rangle$ in Fig. 8b.

To deconvolve the droplet shape from the droplet distribution, we averaged D and θ as functions of the shear rate $|\dot{\gamma}|$ at the droplet center-of-mass using the flow fields measured in the simulations (Fig. 4). We then defined a local capillary number using the solution viscosity μ_0 estimated from eq. (10). Figure 9 shows the results of this procedure for the pure solvent and the $M = 80$ polymers with $\phi_\mathrm{p} = 10.0\%$. In each case, the data were well-collapsed across all body forces when plotted against Ca. Moreover, all data nearly collapsed onto a single curve for small Ca, i.e., near the channel centerline. However, there were some noticeable differences at larger Ca for a given f_x, particularly in θ. These deviations corresponded to larger $\dot{\gamma}$ and droplet positions closer to the channel walls. This discrepancy then may be connected to wall effects on the droplet and larger non-Newtonian effects in the polymer solution in that regime.

The droplet deformation D increased monotonically with shear rate (Fig. 9a). The solid line corresponds to Taylor's prediction with $\lambda \approx 1$. (Including the polymer contribution in the viscosity ratio made less than a 1% difference to the slope of the curve.) The measured deformation was typically larger than predicted by Taylor's theory, in good agreement with previous experimental and numerical studies of confined droplets in Newtonian and non-Newtonian fluids,[93,94] and it never reached zero even as Ca $\to 0$ due to the finite size of the droplet in the parabolic flow. In contrast to D, the inclination angle θ showed a maximum at intermediate Ca (Fig. 9b). This non-monotonic shape is not predicted for droplets confined in simple shear,[91–93] and so is likely due to the parabolic flow field. On visual inspection of the trajectories, the change in orientation with the flow appeared to be due to alignment of the droplet with the walls, but more alignment is also expected at higher Ca.[56,93,94]

Other than these boundary effects, we found that the droplet shape was not strongly influenced by the presence of the polymers in solution. Instead, the deformation and orientation correlated strongly with the shear rate due to the imposed flow. The primary roles of the polymers in setting the average deformation (Fig. 8) were then as viscosity modifiers, altering the flow field (Fig. 4) for a given body force, and as focusers for the droplet, which caused the droplet to experience a given shear rate with higher probability.

Conclusions

We used dissipative particle dynamics computer simulations to show that a Brownian droplet in a dilute polymer solution migrates toward the center of a parallel-plate microchannel under pressure-driven flow. Similar to a small rigid colloid in a polymer solution, the droplet had a distribution of positions in the channel that sharpened near the center for longer polymer chains at higher concentrations. However, the dependence of this distribution on the flow rate was more complex than for the rigid colloid due to the deformability of the droplet, which induced cross-stream migration even in the absence of polymer and also set an upper limit on the accessible flow rate for stretching the polymer chains in order to avoid droplet breakup. Interestingly, the viscoelastic focusing mechanism was robust to the droplet viscosity ratio with the solvent for the flow conditions tested. The average droplet shape depended on the droplet distribution because the local droplet deformation was controlled by the shear rate (capillary number). Our simulations demonstrate the applicability of the viscoelastic focusing mechanism for small Brownian droplets that are comparable in size to the polymer chains in the viscoelastic fluid.

Polymer-induced migration may play an important role in droplet migration and mobility in small channels flooded with complex fluids, such as those encountered in oil recovery from geological formations or in membrane filtration. In this work, we have neglected polymer solubility and adsorption with the droplet, the presence of surfactants, complex microchannel boundaries, and collective interactions between droplets at finite concentration. Such effects are surely present in many applications, and an intriguing avenue of future research is to determine how they may assist or hinder polymer-induced droplet migration in microchannels. Viscoelastic focusing will likely also influence the migration of other rigid and deformable objects in these complex fluid mixtures, including colloids, star polymers,[96] dendrimers, cells, and micelles. Controlling the distribution of these objects in a mixture through general inertial and viscoelastic focusing mechanisms presents an opportunity to effect a separation.

Conflicts of interest

There are no conflicts to declare.

Acknowledgements

We happily thank Florian Müller-Plathe and Athanassios Panagiotopoulos for discussions inspiring this research. Work by M.P.H. was supported as part of the Center for Materials for Water and Energy Systems, an Energy Frontier Research Center funded by the U.S. Department of Energy, Office of Science, Basic Energy Sciences under Award No. DE-SC0019272. T.M.T. acknowledges financial support from the Welch Foundation (Grant No. F-1696), and A.N. acknowledges financial support from the German Research Foundation (DFG) under Project No. NI 1487-2/1. The simulations are part of the Blue Waters sustained-petascale computing project, which is supported by the National Science Foundation (awards OCI-0725070 and ACI-1238993) and the state of Illinois. Blue Waters is a joint effort of the University of Illinois at Urbana-Champaign and its National Center for Supercomputing Applications.

References

1 H. A. Stone and S. Kim, *AIChE J.*, 2001, **47**, 1250–1254.
2 H. A. Stone, A. D. Stroock and A. Ajdari, *Annu. Rev. Fluid Mech.*, 2004, **36**, 381–411.
3 A. A. S. Bhagat, S. S. Kuntaegowdanahalli and I. Papautsky, *Phys. Fluids*, 2008, **20**, 101702.
4 S. C. Hur, N. K. Henderson-MacLennan, E. R. B. McCabe and D. Di Carlo, *Lab Chip*, 2011, **11**, 912–920.
5 J. C. Giddings, *Science*, 1993, **260**, 1456–1465.
6 A. Kumar and M. D. Graham, *Phys. Rev. Lett.*, 2012, **109**, 108102.
7 A. Kumar and M. D. Graham, *Soft Matter*, 2012, **8**, 10536–10548.
8 D. W. Green and G. P. Willhite, in *Enhanced Oil Recovery*, Society of Petroleum Engineers, 1998, pp. 239–300.
9 L. A. Wilson Jr., in *Improved Oil Recovery by Surfactant and Polymer Flooding*, Academic Press, 1977, pp. 1–26.
10 M. A. Tehrani, *J. Rheol.*, 1996, **40**, 1057–1077.
11 A. Y. Fu, C. Spence, A. Scherer, F. H. Arnold and S. R. Quake, *Nat. Biotech.*, 1999, **17**, 1109–1111.
12 A. E. Cohen, *Phys. Rev. Lett.*, 2005, **94**, 118102.
13 H. Lee, A. M. Purdom and R. M. Westervelt, *Appl. Phys. Lett.*, 2004, **85**, 1063–1065.
14 S. Das, S. Mandal and S. Chakraborty, *J. Fluid Mech.*, 2018, **835**, 170–216.
15 S. Das and S. Chakraborty, *Phys. Rev. Fluids*, 2018, **3**, 103602.
16 A. Karimi, S. Yazdi and A. M. Ardekani, *Biomicrofluidics*, 2013, **7**, 021501.
17 H. Amini, W. Lee and D. Di Carlo, *Lab Chip*, 2014, **14**, 2739–2761.
18 L. G. Leal, *Ann. Rev. Fluid Mech.*, 1980, **12**, 435–476.
19 H. A. Stone, *J. Fluid Mech.*, 2000, **409**, 165–183.
20 J.-P. Matas, J. F. Morris and É. Guazzelli, *J. Fluid. Mech.*, 2004, **515**, 171–195.
21 D. Di Carlo, D. Irimia, R. G. Tompkins and M. Toner, *Proc. Natl. Acad. Sci. USA*, 2007, **104**, 18892–18897.
22 G. Segré and A. Silberberg, *Nature*, 1961, **189**, 209–210.
23 B. P. Ho and L. G. Leal, *J. Fluid Mech.*, 1974, **65**, 365–400.
24 D. Di Carlo, J. F. Edd, K. J. Humphry, H. A. Stone and M. Toner, *Phys. Rev. Lett.*, 2009, **102**, 094503.
25 P. C.-H. Chan and L. G. Leal, *J. Fluid Mech.*, 1979, **92**, 131–170.
26 C. A. Stan, L. Guglielmini, A. K. Ellerbee, D. Caviezel, H. A. Stone and G. M. Whitesides, *Phys. Rev. E*, 2011, **84**, 036302.
27 C. A. Stan, A. K. Ellerbee, L. Guglielmini, H. A. Stone and G. M. Whitesides, *Lab Chip*, 2013, **13**, 365–376.
28 D. Legendre and J. Magnaudet, *Phys. Fluids*, 1997, **9**, 3572–3574.
29 P. G. Saffman, *J. Fluid Mech.*, 1965, **22**, 385–400.
30 P. G. Saffman, *J. Fluid Mech.*, 1968, **31**, 624.
31 A. Karnis, H. L. Goldsmith and S. G. Mason, *Can. J. Chem. Eng.*, 1966, **44**, 181–193.
32 S. Mortazavi and G. Tryggvason, *J. Fluid Mech.*, 2000, **411**, 325–350.
33 X. Chen, C. Xue, L. Zhang, G. Hu, X. Jiang and J. Sun, *Phys. Fluids*, 2014, **26**, 112003.
34 D.-y. Pan, Y.-q. Lin, L.-x. Zhang and X.-m. Shao, *J. Hydrodyn., Ser. B*, 2016, **28**, 702–708.
35 R. L. Marson, Y. Huang, M. Huang, T. Fu and R. G. Larson, *Soft Matter*, 2018, **14**, 2267–2280.
36 G. D'Avino, F. Greco and P. L. Maffettone, *Ann. Rev. Fluid Mech.*, 2017, **49**, 341–360.
37 A. M. Leshansky, A. Bransky, N. Korin and U. Dinnar, *Phys. Rev. Lett.*, 2007, **98**, 234501.
38 A. Karnis and S. G. Mason, *Trans. Soc. Rheo.*, 1966, **10**, 571–592.
39 F. Gauthier, H. L. Goldsmith and S. G. Mason, *Rheo. Acta*, 1971, **10**, 344–364.
40 F. Gauthier, H. L. Goldsmith and S. G. Mason, *Trans. Soc. Rheo.*, 1971, **15**, 297–330.
41 J. Y. Kim, S. W. Ahn, S. S. Lee and J. M. Kim, *Lab Chip*, 2012, **12**, 2807–2814.
42 B. Kim and J. M. Kim, *Biomicrofluidics*, 2016, **10**, 024111.
43 G. D'Avino, G. Romeo, M. M. Villone, F. Greco, P. A. Netti and P. L. Maffettone, *Lab Chip*, 2012, **12**, 1638–1645.
44 I. De Santo, G. D'Avino, G. Romeo, F. Greco, P. A. Netti and P. L. Maffettone, *Phys. Rev. Appl.*, 2014, **2**, 064001.
45 A. Nikoubashman, N. A. Mahynski, A. H. Pirayandeh and A. Z. Panagiotopoulos, *J. Chem. Phys.*, 2014, **140**, 094903.
46 A. Nikoubashman, N. A. Mahynski, M. P. Howard and A. Z. Panagiotopoulos, *J. Chem. Phys.*, 2014, **141**, 149906.
47 M. P. Howard, A. Z. Panagiotopoulos and A. Nikoubashman, *J. Chem. Phys.*, 2015, **142**, 224908.

48 M. Trofa, M. Vocciante, G. D'Avino, M. A. Hulsen, F. Greco and P. L. Maffettone, *Comput. Fluids*, 2015, **107**, 214–223.

49 C. Prohm, M. Gierlak and H. Stark, *Eur. Phys. J. E*, 2012, **35**, 80.

50 M. E. Mackay, T. T. Dao, A. Tuteja, D. L. Ho, B. Van Horn, H.-C. Kim and C. J. Hawker, *Nat. Mater.*, 2003, **2**, 762–766.

51 I. Y. Wong, M. L. Gardel, D. R. Reichman, E. R. Weeks, M. T. Valentine, A. R. Bausch and D. A. Weitz, *Phys. Rev. Lett.*, 2004, **92**, 178101.

52 A. Tuteja, M. E. Mackay, S. Narayanan, S. Asokan and M. S. Wong, *Nano Lett.*, 2007, **7**, 1276–1281.

53 R. Poling-Skutvik, R. Krishnamoorti and J. C. Conrad, *ACS Macro Lett.*, 2015, **4**, 1169–1173.

54 R. Chen, R. Poling-Skutvik, A. Nikoubashman, M. P. Howard, J. C. Conrad and J. C. Palmer, *Macromolecules*, 2018, **51**, 1865–1872.

55 R. Chen, R. Poling-Skutvik, M. P. Howard, A. Nikoubashman, S. A. Egorov, J. C. Conrad and J. C. Palmer, *Soft Matter*, 2019, 10.1039/C8SM01834K.

56 S. Guido, *Current Opinion in Colloid & Interface Science*, 2011, **16**, 61–70.

57 A. Gupta and M. Sbragaglia, *Phys. Rev. E*, 2014, **90**, 023305.

58 N. Wang, H. Liu and C. Zhang, *J. Rheol.*, 2017, **61**, 741–758.

59 R. Cardinaels and P. Moldenaers, *Rheol. Acta*, 2010, **49**, 941–951.

60 P. J. Hoogerbrugge and J. M. V. A. Koelman, *Europhys. Lett.*, 1992, **19**, 155–160.

61 P. Español and P. Warren, *Europhys. Lett.*, 1995, **30**, 191–196.

62 R. D. Groot and P. B. Warren, *J. Chem. Phys.*, 1997, **107**, 4423–4435.

63 D. C. Visser, H. C. J. Hoefsloot and P. D. Iedema, *J. Comput. Phys.*, 2006, **214**, 491–504.

64 X. Fan, N. Phan-Thien, S. Chen, X. Wu and T. Y. Ng, *Phys. Fluids*, 2006, **18**, 063102.

65 J. A. Anderson, C. D. Lorenz and A. Travesset, *J. Comput. Phys.*, 2008, **227**, 5342–5359.

66 J. Glaser, T. D. Nguyen, J. A. Anderson, P. Lui, F. Spiga, J. A. Millan, D. C. Morse and S. C. Glotzer, *Comput. Phys. Commun.*, 2015, **192**, 97–107.

67 C. L. Phillips, J. A. Anderson and S. C. Glotzer, *J. Comput. Phys.*, 2011, **230**, 7191–7201.

68 J. G. Kirkwood and F. P. Buff, *J. Chem. Phys.*, 1949, **17**, 338–343.

69 D. Frenkel and B. Smit, *Understanding Molecular Simulation: From Algorithms to Applications*, Academic Press, 2nd edn, 2002, p. 472.

70 F. Müller-Plathe, *Phys. Rev. E*, 1999, **59**, 4894–4898.

71 A. Statt, M. P. Howard and A. Z. Panagiotopoulos, 2018, arXiv:1811.04097.

72 M. Kranenburg, J.-P. Nicolas and B. Smit, *Phys. Chem. Chem. Phys.*, 2004, **6**, 4142–4151.

73 I. V. Pivkin and G. E. Karniadakis, *J. Comput. Phys.*, 2005, **207**, 114–128.

74 D. A. Fedosov, I. V. Pivkin and G. E. Karniadakis, *J. Comput. Phys.*, 2008, **227**, 2540–2559.

75 M. Revenga, I. Zúñiga and P. Español, *Comput. Phys. Commun.*, 1999, **121–122**, 309–311.

76 A. Stukowski, *Modelling Sim. Mater. Sci. Eng.*, 2010, **18**, 015012.

77 C. S. Adorf, P. M. Dodd, V. Ramasubramani and S. C. Glotzer, *Comput. Mater. Sci.*, 2018, **146**, 220–229.

78 M. Rubinstein and R. H. Colby, *Polymer Physics*, Oxford University Press, 2003, pp. 314–318.

79 C.-C. Huang, R. G. Winkler, G. Sutmann and G. Gompper, *Macromolecules*, 2010, **43**, 10107–10116.

80 A. Nikoubashman and M. P. Howard, *Macromolecules*, 2017, **50**, 8279–8289.

81 I. Teraoka, *Polymer Solutions: An Introduction to Physical Properties*, Wiley, New York, 2002.

82 M. Doi and S. F. Edwards, *The Theory of Polymer Dynamics*, Clarendon Press, Oxford, 1986, pp. 97–103.

83 F. Pedregosa, G. Varoquaux, A. Gramfort, V. Michel, B. Thirion, O. Grisel, M. Blondel, P. Prettenhofer, R. Weiss, V. Dubourg, J. Vanderplas, A. Passos, D. Cournapeau, M. Brucher, M. Perrot and E. Duchesnay, *J. Mach. Learn. Res.*, 2011, **12**, 2825–2830.

84 M. Ester, Kriegel, Hans-Peter, J. Sander and X. Xu, Proceedings of the 2nd International Conference on Knowledge Discovery and Data Mining, Portland, OR, 1999, pp. 226–231.

85 S. Asakura and F. Oosawa, *J. Chem. Phys.*, 1954, **22**, 1255–1256.

86 W. B. Russel, D. A. Saville and W. R. Schowalter, *Colloidal Dispersions*, Cambridge University Press, 1989.

87 G. I. Taylor, *Proc. R. Soc. London A*, 1932, **138**, 41–48.

88 G. I. Taylor, *Proc. R. Soc. London A*, 1934, **146**, 501–523.

89 M. Ripoll, R. G. Winkler and G. Gompper, *Phys. Rev. Lett.*, 2006, **96**, 188302.

90 J. M. Rallison and A. Acrivos, *J. Fluid Mech.*, 1978, **89**, 191–200.

91 R. Roscoe, *J. Fluid Mech.*, 1967, **28**, 273–293.

92 C. E. Chaffey and H. Brenner, *J. Colloid Interface Sci.*, 1967, **24**, 258–269.

93 M. Minale, S. Caserta and S. Guido, *Langmuir*, 2010, **26**, 126–132.

94 A. Gupta, M. Sbragaglia and A. Scagliarini, *J. Comput. Phys.*, 2015, **291**, 177–197.

95 D. Pan, N. Phan-Thien and B. C. Khoo, *J. Non-Newtonian Fluid Mech.*, 2014, **212**, 63–72.

96 D. Srivastva and A. Nikoubashman, *Polymers*, 2018, **10**, 599.

Dilute polymer solutions under pressure-driven flow can drive cross-stream migration of a small Brownian droplet to the centerline of a planar microchannel.